Shrinkage and expansion of discharge areas in plasma discharge devices having complex oxide protective layers

Takeda, Eiji ; Zukawa, Takehiro ; Ishibashi, Tasuku ; Yoshino, Kyohei ; Kosugi, Naoki ; Morita, Yukihiro ; Fujii, Minoru

(Citation)
Journal of Physics and Chemistry of Solids,130:172-179

(Issue Date)
2019-07

(Resource Type)
journal article

(Version)
Accepted Manuscript

Shrinkage and expansion of discharge areas in plasma discharge devices having complex oxide protective layers

Eiji Takeda[1]

Department of Electric and Electronic Engineering, Graduate School of Engineering, Kobe University, 1-1 Rokkoudai, Nada, Kobe City, Hyogo 657-8501, Japan

Sensing Solution Development Center, Engineering Division, Automotive & Industrial Systems Company, Panasonic Corporation, 1006 Kadoma, Kadoma City, Osaka 571-8506, Japan

Takehiro Zukawa

Institute for Sensors and Devices, Technology Innovation Division, Panasonic Corporation, 1006 Kadoma, Kadoma City, Osaka 571-8508, Japan

Tasuku Ishibashi

Housing Systems Business Division, Eco Solutions Company, Panasonic Corporation, 1048 Kadoma, Kadoma City, Osaka 571-8686, Japan

Kyohei Yoshino

Automotive Infotainment Systems Business Division, Automotive & Industrial Systems Company, Panasonic Corporation, 4261 Ikonobe, Tsuzuki, Yokohama City, Kanagawa 224-8520, Japan

Naoki Kosugi

Innovation Center, Connected Solutions Company, Panasonic Corporation, 3-1-1 Yagumo-naka-machi, Moriguchi City, Osaka 570-8501, Japan

Yukihiro Morita

Institute for Sensors and Devices, Technology Innovation Division, Panasonic Corporation, 1006 Kadoma, Kadoma City, Osaka 571-8508, Japan

Panasonic Device Science Research Alliance Laboratory, Graduate School of Engineering, Osaka University, 1-1 Yamadaoka, Suita City, Osaka 565-0871, Japan

Minoru Fujii

[1]Electronic mail: takeda.eiji@jp.panasonic.com

Department of Electric and Electronic Engineering, Graduate School of Engineering, Kobe University, 1-1 Rokkoudai, Nada, Kobe City, Hyogo 657-8501, Japan

Abstract

The modification of the discharge area in flat panel plasma discharge devices having a complex metal oxide protective layer on prolonged aging was demonstrated. In the case of a (Mg,Ca)O protective layer, the discharge area shrank with the discharge intensity reduced during aging. The CaO concentration was increased at the layer surface by the preferential sputtering of MgO, which is promoted by higher Xe levels in the discharge gas. These results indicate that a modified distribution of the secondary electron emission property at the surface due to the compositional change leads to the shrinkage of the discharge area. This work also demonstrated that reducing the permittivity of the dielectric layer under the protective layer expanded the discharge area, thus suppressing the degradation of the discharge intensity in the plasma discharge devices.

Keywords: plasma discharge, discharge area, complex oxide, preferential sputtering, sputtering yield
PACS: 52.25.-b, 68.35.-p, 79.20.-m

1. Introduction

Dielectric barrier discharge (DBD) is a well-known technology that allows the efficient generation of plasmas to obtain mercury-free ultraviolet sources [1, 2, 3]. As examples, Xe plasmas have been applied to cylindrical fluorescent lamps and flat panel plasma discharge devices such as plasma displays [4, 5, 6], planar lighting fixtures [7, 8, 9], and plate-type virus inactivation units [10, 11, 12]. These devices are alternatives to light emitting diodes (LEDs), which are also effective light sources [13]. Plasma discharge devices have significant size expansion potential and can be fabricated at reasonable production costs. However, the luminous efficiency of plasma discharge devices is limited to several tens of lm/W [7], which is inferior to that of LEDs (which can generate over 100 lm/W) [13, 14]. Therefore, improving the luminous efficiency of

plasma discharge devices would be highly beneficial in terms of expanding the potential market.

One key means of enhancing luminous efficiency is increasing the electron emission efficiency from the dielectric electron emitter, which plays an important role in generating and sustaining the Xe plasma. In such devices, a Ne:Xe gas mixture is often used as the discharge gas to reduce the discharge voltage and generate vacuum ultraviolet (VUV) radiation via the Penning effect. A higher Xe content in the plasma discharge device improves the VUV generation efficiency, although the discharge voltage increases [15, 16, 17]. The discharge voltage greatly depends on the ion-induced secondary electron emission coefficient (γ) for the oxide layer applied to the dielectric layer to protect the front panel electrodes from discharge sputtering [18]. MgO is commonly used as the protective layer because of its relatively high chemical stability and suitable γ value for Ne, although its γ value is low for Xe. Therefore, materials having higher γ values for Xe than MgO are required to realize low discharge voltages in association with high Xe levels in plasma discharge devices.

Higher γ materials that have been assessed for use as protective layers in plasma discharge devices include other alkaline earth metal oxides, such as CaO, SrO, and BaO, which have narrower band gaps and lower electron affinities in this order [19]. These properties in turn increase their γ values with Xe due to efficient electron emission via the Auger neutralization process [20, 21]. However, as a result of lowering the Madelung potentials at the surfaces, the reactivity of surface O^{2-} ions on these materials is greatly enhanced [22, 23]. Therefore, these compounds readily react with H_2O and CO_2 in the ambient atmosphere to form carbonation products [24], which widens the band gap of the material and reduces the γ value for Xe [25]. For this reason, it is difficult to find practical applications for alkaline earth metal oxides other than MgO as protective layers in plasma discharge devices.

In order to improve the chemical properties of these alkaline earth metal oxides, more complex metal oxides, such as (Mg,Ca)O [26, 27, 28], (Mg,Sr)O [29, 30, 31], (Mg,Ca,Sr)O [30, 32], (Mg,Ba)O [33], and other materials [34, 35, 36] have been extensively studied. Lower discharge voltages have been realized even for large devices using complex metal oxides for protective layers rather than the conventional MgO. However, the discharge behavior by complex metal oxide protective layers and the changes in the panel characteristics upon prolonged aging have yet to be assessed.

In this study, we investigated the discharge behavior of flat panel plasma

discharge devices with a complex metal oxide protective layer under prolonged aging. Plasma display panels were employed as model Xe DBD devices. The results demonstrate the shrinkage and expansion of the discharge area after aging. Analyses of the sputtered protective layer surfaces reveal the mechanisms of the discharge modifications. Moreover, pixel structures that effectively suppress the degradation of the device efficiency are proposed.

2. Experimental Methods

The discharge behavior of plasma discharge devices with a complex oxide protective layer during aging was investigated using 42-inch full-high definition alternating current plasma display panels. (Mg,Ca)O was employed as the complex oxide protective layer because this is currently considered to be the most promising material in devices having high Xe concentrations in the discharge gas (so as to achieve both increased VUV radiation generation efficiency and low discharge voltage) [26, 27, 28]. The improved performance by (Mg,Ca)O is due to the higher ion-induced secondary electron emission characteristics compared to those of MgO for not only plasma displays but also other plasma discharge devices. A (Mg,Ca)O film with a thickness of 800 nm was deposited by electron beam evaporation on the dielectric layer. The permittivity and thickness of the dielectric layer (ϵ_d and d_d) were 11.3 and 39 μm, respectively. The evaporation targets were sintered mixtures of MgO and CaO. The CaO concentration in the resulting films was in the range from 3.0 to 17.8 mol % depending on the ratio of the two oxides in the target. Following (Mg,Ca)O deposition, MgO powder was dispersed on the protective layer to improve the statistical discharge delay [37]. A Ne:Xe mixture was used as a discharge gas, with the Xe concentration of 15 % and at the pressure in the panel of 450 Torr. The specifications of the test panels used in this study are provided in Table 1. Panel aging tests were carried out under accelerated conditions, although the aging times reported herein correspond to the actual operational time spans. The panels were dismantled and then cut into the pieces at the size of a few cm^2 for the following measurement.

The CaO concentration at the surfaces of the (Mg,Ca)O protective layers was estimated by X-ray photoelectron spectroscopy (XPS; PHI Quantera SXM, ULVAC PHI). The samples were excited by a monochromatic X-ray source with an Al Kα line at 1486.7 eV. The sample surfaces were neutralized with a combination of electrons and an Ar^+ beam to suppress charging effects

Table 1: Specifications of the test panels used in this study.

Front Panel	
ITO electrode width	110 μm
Bus electrode width	65 μm
Electrode gap	80 μm
Dielectric layer thickness	39 μm
Protective layer thickness	800 nm
Back Panel	
Address electrode width	65 μm
Dielectric layer thickness	10 μm
Barrier rib height	120 μm
Barrier rib width	40 μm
Phosphor thickness	12 μm
Pixel size	480×160 μm^2

during the XPS analyses [38]. The photoelectron signals from the samples were detected at a take-off angle of 45° using a concentric hemispherical analyzer with a pass energy of 69 eV for Mg photoelectrons and 140 eV for Ca photoelectrons. Mg 2p and Ca 2s photoelectron spectra were analyzed to calculate the CaO concentration. Mg 2p photoelectrons provide one of the most intense lines for Mg. For Ca, Ca 2s line was employed because the kinetic energy of the most intense Ca 2p lines overlaps with that of Mg KLL Auger electrons when using the Al Kα line as an X-ray excitation source. Mapping measurements of the CaO concentration were carried out by scanning a focused X-ray beam with a spot size of 18 μm at 20 μm intervals. A software package intended for XPS analysis (MultiPak, ULVAC PHI) was used to subtract the Shirley background signals for all photoelectron spectra [39]. Mg 2p and Ca 2s photoelectron signal intensities were corrected by setting the relative sensitivity factors over the regions being assessed to 13.546 and 76.596 provided by the MultiPak software, respectively.

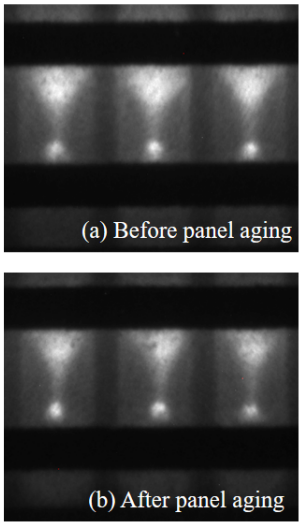

Figure 1: Images showing the near infrared emission associated with the Xe discharge from pixels in panels with a (Mg,Ca)O protective layer (a) before and (b) after aging.

3. Results and Discussion

We carried out 2500 h aging tests using panels with (Mg,Ca)O protective layers and compared the discharge behavior before and after the aging. Figures 1(a) and (b) show discharge images of panel pixels with (Mg,Ca)O protective layers before and after aging at the same applied voltage, respectively. These images were obtained by capturing the near infrared emission primarily at 823 and 828 nm associated with the $Xe(6p[3/2]_2) \rightarrow Xe(6s[3/2]_2)$ and $Xe(6p[1/2]_0) \rightarrow Xe(6s[3/2]_1)$ transitions [40], respectively, using a gated ICCD apparatus comprising an image intensifier (M7971-01, Hamamatsu Photonics) and a digital CCD camera (C8484, Hamamatsu Photonics). In these images, the white region represents the near infrared emission resulting from discharge, while the horizontal black lines are bus electrodes. Shrinkage of the discharge area after the prolonged aging is evident.

To assess the change of the discharge area quantitatively, we defined the discharge area as the number of ICCD camera pixels for which the signal was more than half the maximum infrared emission intensity within the panel. Figure 2 plots the relationship between the normalized discharge area and normalized peak and integrated discharge intensities with respect to the initial area and intensity during aging. The solid and dotted lines correspond

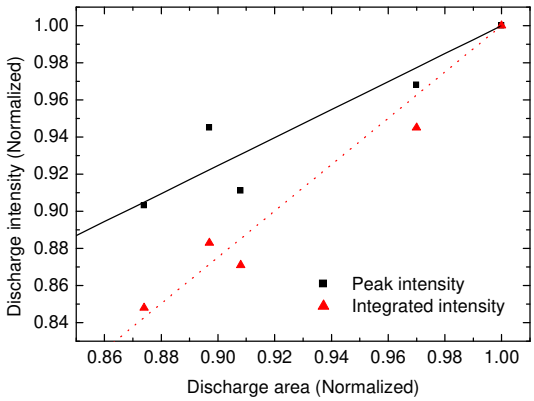

Figure 2: (Color online) Discharge intensities (normalized with respect to the initial intensities) as a function of the discharge area (normalized with respect to the initial area). Squares and triangles correspond to the peak and integrated intensities, respectively, and solid and dotted lines indicate linear fits for the peak and integrated intensities, respectively.

to linear fits for the peak and integrated intensities, respectively. As the discharge area shrinks, both the peak and integrated intensities become smaller. Therefore, the shrinkage of the discharge area is the cause of the reduction of the panel luminous efficiency. Luminous efficiency is also reduced in the case of a conventional MgO protective layer by aging. However, the shrinkage of the discharge area has not been observed.

We investigated the shrinkage of the discharge area associated with the (Mg,Ca)O protective layer by dismantling the aged panels and by analyzing the surfaces using optical microscope and XPS. The results are shown in Figs. 3(a), (b), and (c) for panel aging times of 100, 800, and 2500 h, respectively. Discharge trace images acquired with a digital optical microscope (VHX-500, Keyence) are shown in the upper part, while maps of the surface CaO concentration obtained by XPS at the same areas are shown in the lower part. In the optical microscope images, the black dots are dispersed MgO and the broad horizontal shadows are the embedded bus electrodes. The bulk CaO concentration in the (Mg,Ca)O protective layer in Fig. 3 is ~ 11 mol %. It is evident that the surface CaO concentration is greater in the sputtered regions and increases during aging.

The secondary electron emission coefficient (γ) for the protective layer

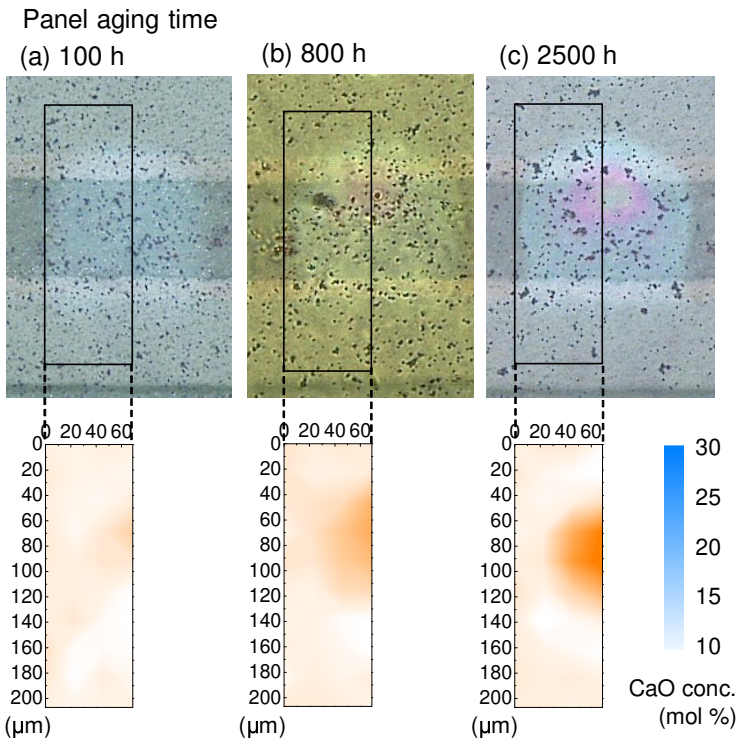

Figure 3: (Color online) Optical microscope images and XPS maps of the CaO concentration in the discharge traces of (Mg,Ca)O protective layers following aging times of (a) 100, (b) 800, and (c) 2500 h.

is expected to be enhanced in the region of increased CaO concentration [41]. In the region, high γ leads to localized sputtering of the protective layer, resulting in further local increase of the CaO concentration. This process proceeds until the CaO concentration becomes stable. In order to investigate the cause of the CaO concentration increase, we evaluated CaO concentrations after 2500 h aging for (Mg,Ca)O with different initial CaO concentration. The results are plotted in Fig. 4. As expected, higher initial CaO concentration results in higher final CaO concentration.

If we assume that the increase in the CaO concentration is caused by the preferential sputtering of MgO within a (Mg,Ca)O protective layer, the temporal changes in the MgO and CaO concentrations ($C_{MgO}(t)$ and $C_{CaO}(t)$,

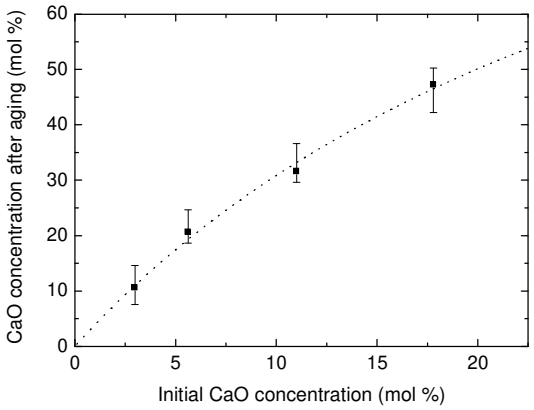

Figure 4: CaO concentration in (Mg,Ca)O protective layers after 2500 h aging, as a function of the initial CaO concentration. Square plots correspond to experimental data, while the dotted line indicates the results obtained by calculations using Eq. (4), setting Y_{MgO}/Y_{CaO} to 4.02.

respectively) on the surface of the protective layer can be expressed as [42]

$$C_{MgO}(t) = N_{MgO} \exp(-t/\tau) + N_{MgO} w_{CaO} \tau \left[1 - \exp(-t/\tau)\right], \qquad (1)$$

and

$$C_{CaO}(t) = N_{CaO} \exp(-t/\tau) + N_{CaO} w_{MgO} \tau \left[1 - \exp(-t/\tau)\right], \qquad (2)$$

where $C_{MgO}(t) + C_{CaO}(t) = 1$ and $\tau = (N_{MgO} w_{CaO} + N_{CaO} w_{MgO})^{-1}$. Here, N_{MgO} and N_{CaO} are the bulk concentrations of MgO and CaO, respectively, where $N_{MgO} + N_{CaO} = 1$, and w_{MgO} and w_{CaO} are the MgO and CaO sputtering rates, respectively. These equations are based on several assumptions. Firstly, a (Mg,Ca)O film is a mixture of MgO and CaO. Secondly, only the outermost layer is sputtered while the material below is not modified. Lastly, the sputtering yields of MgO and CaO (Y_{MgO} and Y_{CaO}, respectively) are independent of the ratio of MgO to CaO.

From Eqs. (1) and (2), the steady-state MgO-to-CaO concentration ratio (C_{MgO}/C_{CaO}) can be expressed as

$$\frac{C_{MgO}(t \to \infty)}{C_{CaO}(t \to \infty)} = \frac{N_{MgO}}{N_{CaO}} \frac{w_{CaO}}{w_{MgO}} = \frac{N_{MgO}}{N_{CaO}} \frac{Y_{CaO}}{Y_{MgO}}, \qquad (3)$$

which leads to

$$C_{CaO}(t \to \infty) = \left(\frac{1 - N_{CaO}}{N_{CaO}} \frac{Y_{CaO}}{Y_{MgO}} + 1 \right)^{-1}. \quad (4)$$

The dotted curve in Fig. 4 is the result of the fitting of the data with Eq. (4) by using Y_{MgO}/Y_{CaO} as a free fitting parameter. The best result is obtained when Y_{MgO}/Y_{CaO} is 4.02.

The MgO and CaO sputtering yields are affected by both the ionic species (Ne^+ and Xe^+) and the incident ion energies. Since the ions in the panel pixels have an energy distribution from several tens to a hundred and several tens of eV [43, 44, 45], the average sputtering yield (Y') for a given ion is expressed as [46]

$$Y' = \int_0^V Y(E) g(E) dE, \quad (5)$$

where $Y(E)$ is the sputtering yield as a function of an incident ion energy E, $g(E)$ is the normalized ion flux energy distribution with respect to the total ion flux, and V is the cathode fall potential, which is approximately equal to the voltage applied to the panel. If the mean free path for the symmetric charge transfer (l) is much shorter than the length of the cathode fall region (L), $g(E)$ can be expressed as [47]

$$g(E) = \frac{L}{2l} \frac{1}{V} \exp\left[- \left(\frac{L}{2l} \frac{E}{V} \right) \right]. \quad (6)$$

The mean free path l is obtained by $(N\sigma)^{-1}$ [46], where N is the discharge gas density and σ is the cross section of symmetric charge transfer between ions and their parent neutral atoms. The values of the σ are reported as 2.0×10^{-15} cm^2 for Ne-Ne^+ and 8.0×10^{-15} cm^2 for Xe-Xe^+ [44], thus the L/l values of Ne^+ and Xe^+ are 49.2 and 34.8 in the case of a Xe content in the discharge gas of 15 % and a gas pressure of 450 Torr assuming $L =$ 20 μm, respectively [46]. Figure 5 shows the estimated energy distributions for Ne^+ and Xe^+ fluxes arriving at (Mg,Ca)O layer surface at the applied firing voltage of 360 V using Eq. (6). The energy distribution of the Ne^+ flux is less than that of the Xe^+ due to the greater probability of charge transfer collisions for Ne^+ [48]. Although the approximative values in Fig. 5 are somewhat different from the actual values especially at the high-energy

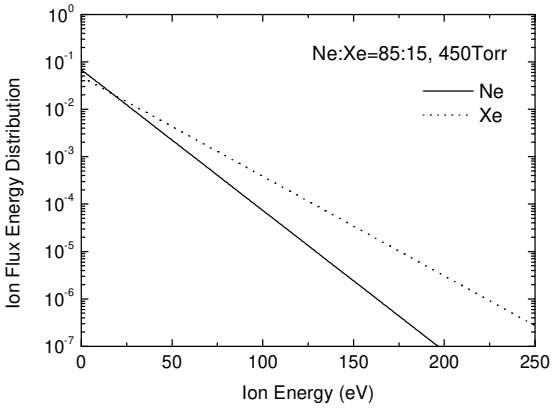

Figure 5: Estimated energy distributions for Ne^+ and Xe^+ fluxes arriving at the (Mg,Ca)O layer surface in the case of a Xe content in the discharge gas of 15 % and a gas pressure of 450 Torr at the applied voltage of 360 V using Eq. (6).

region due to frequent charge exchange collisions, the effects are limited for the following calculations because of much low amounts of the ions with high energy [49].

The MgO and CaO sputtering yields for low-energy ion bombardment have been experimentally determined for various noble gas ions [50, 51, 52]. In these prior studies, the experimentally determined dependence of the sputtering yield on the normally incident ion energy ($Y(E)$) are fitted using the formula

$$Y(E) = a\left(1 - \sqrt{\frac{E_0}{E}}\right)^{\frac{5}{2}}\left[1 + b\left(\sqrt{\frac{E}{E_0}} - 1\right)\right]. \tag{7}$$

In the case of Ne^+, a, b and E_0 are 1.88, -0.148 and 66.7 eV for MgO, and 0.0284, 15 and 53.5 eV for CaO, respectively. In the case of Xe^+, a, b and E_0 are 0.119, 8.96 and 58.4 eV for MgO, and 0.0781, 13.8 and 84.3 eV for CaO, respectively. MgO is sputtered to a greater extent than CaO due to its lower molecular mass (i.e., 40.3 g/mol for MgO and 56.1 g/mol for CaO).

$Y(E)g(E)$ in Eq. (5) can be calculated from the $Y(E)$ data in Refs. [50, 51] and the $g(E)$ values in Fig. 5. Figures 6(a) and (b) show the calculated $Y(E)g(E)$ of MgO and CaO for Ne^+ and Xe^+, respectively. It

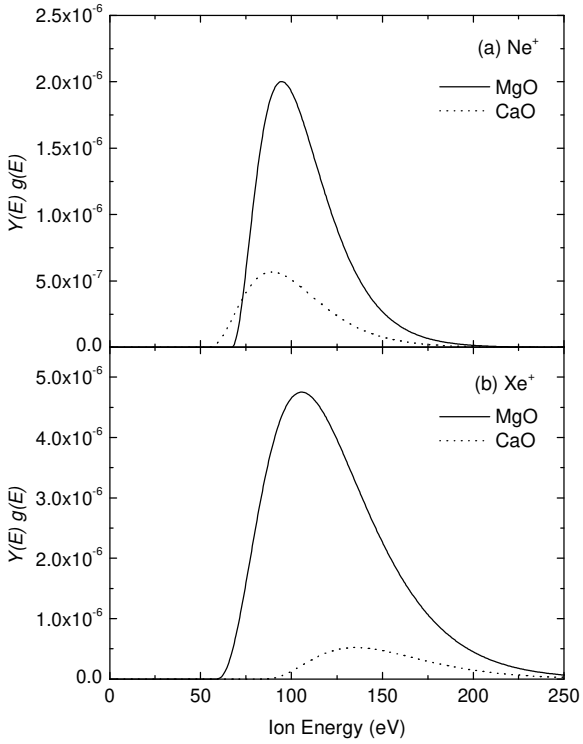

Figure 6: Calculated distribution of $Y(E)g(E)$ for MgO and CaO in conjunction with (a) Ne^+ and (b) Xe^+ sputtering.

has wider distribution in Xe^+ than in Ne^+ due to larger amounts of high energy Xe^+ as can be seen in Fig. 5, which indicates that Xe^+ has a greater effect on the sputtering yield of (Mg,Ca)O. The $Y(E)g(E)$ values for Ne^+ in the present study are much lower than those in Ref. [46] even at the similar discharge gas conditions, which arises from the different sputtering yields applied to the calculations. The sputtering yields applied in this study have higher sputtering threshold energies and lower amounts in the low energy region, where much more of the ion flux exist, resulting in the lower $Y(E)g(E)$ values in this work compared with those in Ref. [46].

The average sputtering yield per panel pixel ($Y'^{\,panel}$) can be expressed

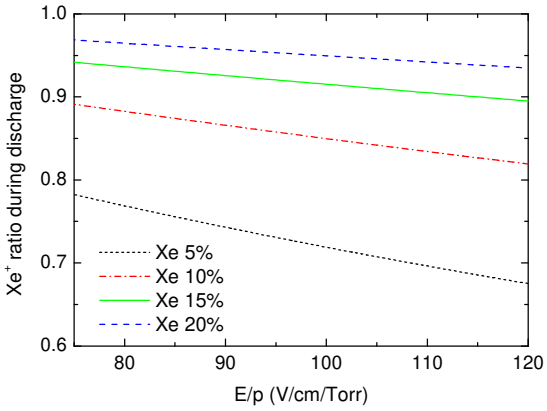

Figure 7: (Color online) The Xe^+ ratios during the discharge ($N_{Xe^+}/(N_{Ne^+} + N_{Xe^+})$) at various Xe concentrations as a function of E/p.

as

$$Y'^{\,panel} = Y'^{\,Ne^+} \frac{N_{Ne^+}}{N_{Ne^+} + N_{Xe^+}} + Y'^{\,Xe^+} \frac{N_{Xe^+}}{N_{Ne^+} + N_{Xe^+}}, \tag{8}$$

where $Y'^{\,Ne^+}$ and $Y'^{\,Xe^+}$ are the Y' values for Ne^+ and Xe^+ sputtering, respectively, and N_{Ne^+} and N_{Xe^+} are the quantities of Ne^+ and Xe^+ ions generated during discharge, respectively. The ion ratio during the discharge can be estimated by calculating the ionization coefficients for Ne and Xe using the Boltzmann equation solver (Bolsig+, Gerjan Hagelaar) [53]. Figure 7 plots the Xe^+ ratios during the discharge ($N_{Xe^+}/(N_{Ne^+} + N_{Xe^+})$) at various Xe concentrations as a function of E/p, where E and p indicate the electric field intensity in a pixel and the pressure of the discharge gas, respectively. These plots demonstrate that the Xe^+ ratio increases when E/p decreases. The Xe^+ ratio can be estimated at 0.915 based on the values of Ne:Xe = 85:15 and E/p $\approx$ 100 V/cm/Torr in this study.

The results obtained using Eqs. (5) and (8) for MgO and CaO are summarized in Table 2. The Y_{MgO}/Y_{CaO} resulting from the data in Table 2 is 8.34, which is approximately 2 times larger than the value obtained from Fig. 4. This difference is attributed to several effects. Firstly, the energetic ions in the pixels are predominantly distributed over the range of 10° to 30°

Table 2: Calculation results obtained using Eqs. (5) and (8) for MgO and CaO.

	Y'^{Ne^+}	Y'^{Xe^+}	Y'^{panel}
MgO	9.59×10^{-5}	3.55×10^{-4}	3.33×10^{-4}
CaO	3.11×10^{-5}	4.08×10^{-5}	4.00×10^{-5}

with respect to the surface normal [54], while the ion incidence angle applied for the sputtering yield in this study is 0° with respect to the surface normal. This difference in the incidence angle may modify the sputtering yield [55]. Moreover, especially in the case of low-energy ion bombardment (during which numerous ion fluxes exist in the panel pixel), the sputtering yield is greatly modified by surface charging effects. Carbonation may also modify the MgO sputtering yield similar to the case of hydroxylation reported in Refs. [56, 57]. This effect may be larger in CaO due to the high surface reactivity, leading to significant change of the CaO sputtering yield. Especially in (Mg,Ca)O, it has been demonstrated that carbonation species are predominantly adsorbed at Ca site, but not at Mg site [28]. However, it is difficult to estimate these effects quantitatively because the amounts of the modification of the sputtering yield by ion bombardment with various incidence angles, by surface charging, and by carbonation have yet to be studied for MgO and CaO. Although the sputtering yield ratio from Table 2 is different from the estimated values in Fig. 4 because of these reasons, the good correlation between the experimental and calculated data upon setting Y_{MgO}/Y_{CaO} to 4.02 demonstrates that the increase in the CaO concentration is due to the preferential sputtering.

The effect of the Xe content on this preferential sputtering was assessed by determining Y_{MgO}/Y_{CaO} as a function of the Xe proportion in the Ne:Xe mixed discharge, based on Eq. (7). The estimated Xe^+ ratio during the discharge ($N_{Xe^+}/(N_{Ne^+} + N_{Xe^+})$) at E/p = 100 V/cm/Torr and the normalized Y_{MgO}/Y_{CaO} value with respect to the maximum at an ion bombardment energy of 100 eV for both Ne^+ and Xe^+ are shown in Figs. 8(a) and (b), respectively. The Xe^+ ratio during the discharge reached $\sim$ 1 even at a 60 % Xe content. A Xe^+ bombardment results in preferential MgO sputtering (relative to CaO sputtering) compared with Ne^+ because Xe^+ has a much heavier atomic mass (i.e., 20.2 g/mol for Ne and 131.3 g/mol for Xe). There-

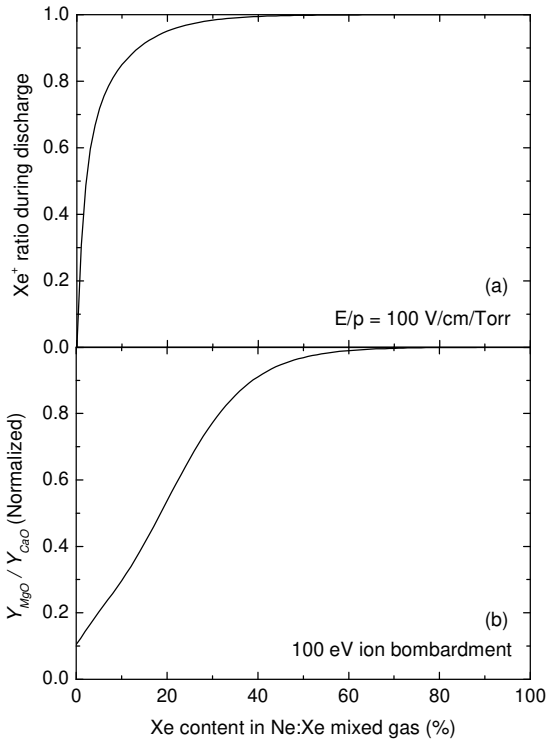

Figure 8: (a) Estimated Xe^+ ratio during the discharge ($N_{Xe^+}/(N_{Ne^+}+N_{Xe^+})$) as a function of the Xe content in the Ne:Xe mixed gas at E/p = 100 V/cm/Torr. (b) Normalized Y_{MgO}/Y_{CaO} values with respect to the maximum as a function of the Xe content in the Ne:Xe mixed gas at an ion bombardment energy of 100 eV for both Ne^+ and Xe^+ with normal incidence, using a formula and parameters described in Refs. [50, 51].

fore, Y_{MgO}/Y_{CaO} increases along with the Xe content but plateaus above 60 % Xe.

As noted above, higher Xe levels increase the VUV output in plasma discharge devices, but also increase the discharge voltage [16, 17]. Thus, high γ materials such as (Mg,Ca)O have been studied as protective layers to suppress increases in the discharge voltage [26, 27, 28]. However, considering the above results, it is apparent that higher Xe levels modify the aging characteristics of panels with a (Mg,Ca)O protective layer based on preferential sputtering. Preferential sputtering also appears for other com-

plex oxide protective layers, including (Mg,Sr)O [29, 30, 31], (Mg,Ca,Sr)O [30, 32], (Mg,Ba)O [33], and (Sr,Ca)O [34, 58, 59], whose sputtering yields and γ for each single metal oxide are clearly different. The degradation of the discharge intensity due to the shrinkage of the discharge area proceeds primarily as a consequence of the preferential sputtering during prolonged aging, even if the initial properties of the panels with a complex metal oxide protective layer are improved by a high Xe content in the discharge gas. This is considered to be a critical point for the practical applications of complex oxide protective layers having high γ.

The practical application of complex oxide protective layers will require improved pixel structures to suppress the shrinkage of the discharge area. Thus, we investigated the discharge area modification upon prolonged aging while varying the initial discharge area. The initial discharge area depends on the geometry of the bus electrodes [60, 61, 62], ϵ_d or d_d [60, 63, 64], and so panels with various ϵ_d, d_d and pixel sizes were fabricated and aged for 2500 h. Figure 9 shows digital optical microscope images of the discharge traces of the protective layers for panels with dielectric layers having ϵ_d and d_d values of 11.3 and 39 μm, and 5.9 and 24 μm, respectively. The firing discharge voltage evidently increases by decreasing ϵ_d or increasing d_d [63]. When ϵ_d was changed from 11.3 to 5.9, d_d was adjusted to keep the equivalent firing voltage. Thus, the results shown in Fig. 9 were obtained under almost the same E/p. In Fig. 9, it is evident that wider regions were sputtered and the maximum sputtered depth decreased with decreasing ϵ_d and d_d. Simulations of the excited states of Xe and the dimer Xe_2^* have shown similar results. The full width at half maximum of the photon flux region becomes much wider upon decreasing ϵ_d while the region becomes narrower upon decreasing d_d [60]. The results shown in Fig. 9 demonstrate that the discharge area can be controlled by changing the dielectric layer.

We assessed the modification of the discharge area after 2500 h aging while adjusting the initial discharge area with various dielectric layers and pixel sizes. The results are shown in Fig. 10. The data above the dotted line demonstrate that the discharge area after aging is wider than the initial discharge area. Below the threshold value of the initial discharge area ($\sim$ 450 in this study), the discharge area after aging is decreased. In contrast, the discharge area after aging is increased above the threshold value. The shrinkage and expansion of the discharge area depending on the size of the initial discharge area are explained below.

Figure 11 presents a schematic of the initial discharge and γ distributions

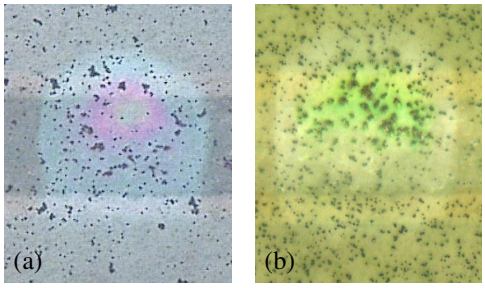

Figure 9: (Color online) Optical microscope images of the discharge traces for panels with different dielectric layers under the (Mg,Ca)O protective layers. The permittivity and thickness of the dielectric layers are (a) 11.3 and 39 μm, and (b) 5.9 and 24 μm, respectively.

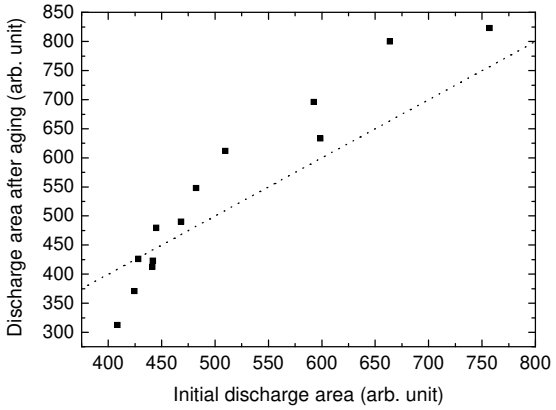

Figure 10: Relationship between the initial discharge area and the discharge area after 2500 h aging for panels with a (Mg,Ca)O protective layer. The data above the dotted line show that the discharge area after aging was wider than the initial discharge area.

in a panel pixel after aging for various ϵ_d and d_d values. In the case that $\epsilon_d = 11.3$ and $d_d = 39$ μm, the initial discharge area becomes narrow. This leads to localized sputtering of the protective layer, thus increasing the CaO concentration and γ due to preferential sputtering. The edge regions exhibit almost no sputtering, and so the difference in γ values between the edge and the center region becomes high, resulting in shrinkage of the discharge

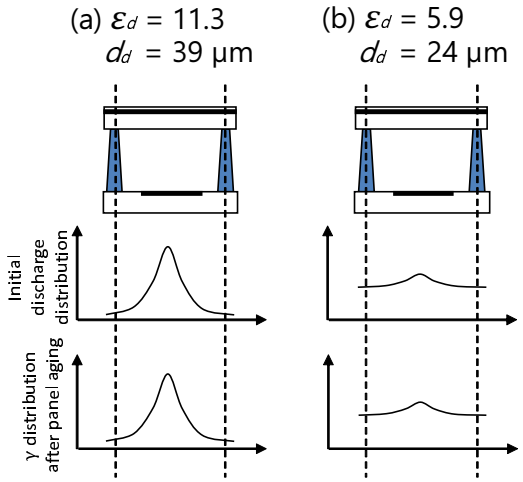

Figure 11: (Color online) Schematic of the discharge and γ distributions in a panel pixel in the cases of (a) $\epsilon_d = 11.3$, $d_d = 39$ μm and (b) $\epsilon_d = 5.9$, $d_d = 24$ μm.

area. In contrast, if ϵ_d is reduced, the initial discharge area is widened. Not only the center regions but also the edge regions are sputtered by the wider discharge to generate a higher γ, thus expanding the discharge area. Therefore, the initial discharge area must be sufficiently wide in order to suppress the shrinkage of the discharge area within the (Mg,Ca)O protective layer.

Finally, we investigated the effects of an initial discharge area on the panel luminous efficiency, which is determined by ϵ_d and d_d values. Figure 12 plots the luminous efficiency (normalized with respect to the initial efficiencies) as a function of the aging time for ϵ_d and d_d values of 11.3 and 39 μm, and 5.9 and 24 μm, respectively. The solid and dotted lines correspond to fitting curves generated using exponential decay functions. The efficiency degradation is clearly slowed down in smaller ϵ_d. The degradation of the panel luminous efficiency during aging is caused due to the decreased phosphor excitation efficiency by prolonged aging [65] and the deterioration of phosphors [66, 67, 68] and protective layers [69, 70] by VUV or discharge irradiation. However, the present work indicates that efficiency loss also arises from a contraction of the discharge area due to preferential sputtering of the protective layer, and can be suppressed by adjusting the initial discharge area due to the modification of the ϵ_d and d_d values.

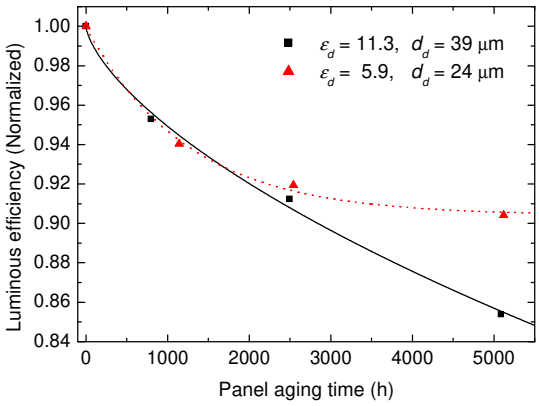

Figure 12: (Color online) Normalized panel luminous efficiency for ϵ_d and d_d values of 11.3 and 39 μm (squares) and 5.9 and 24 μm (triangles). Solid and dotted lines indicate fitting curves generated using exponential decay functions.

4. Conclusions

The discharge modification of panels with (Mg,Ca)O protective layers after prolonged aging was investigated. After aging, shrinkage of the discharge area was observed, and the CaO concentration increased in the sputtered regions on the (Mg,Ca)O protective layer. A comparison between experimental and calculated data indicated that the CaO concentration increased due to the preferential sputtering of MgO in the protective layer in response to low-energy ion bombardment. Therefore, we propose that the reduced discharge arises from variations in the γ distribution in the panel pixels due to the change in the CaO concentration. This preferential sputtering is enhanced by a higher Xe content in the discharge gas and by a smaller E/p value. We also evaluated the discharge modification during prolonged aging due to variations in the initial discharge area, which can be controlled by adjusting the characteristics of the dielectric layer under the protective layer. Reducing ϵ_d was found to expand the discharge area, thus suppressing degradation of the panel luminous efficiency. These results should be valuable during the development and practical application of complex oxide protective layers having high γ values for plasma displays and other plasma discharge devices including a high Xe content together with increased luminous efficiency and a low discharge voltage.

Acknowledgments

This work was primarily performed at the facilities of the PDP Advanced Development Group, PDP Devices Business Unit, Visual Products and Display Devices Business Group, AVC Networks Company, Panasonic Corporation. This research was supported in part by the AVC Devices Development Center, Technology Planning and Development Center, AVC Networks Company, the Image Devices Development Center, Corporate R&D Division, and the Production Engineering Laboratory, Manufacturing Technology and Engineering Division of the Panasonic Corporation.

References

[1] U. Kogelschatz, Dielectric-barrier Discharges: Their History, Discharge Physics, and Industrial Applications, Plasma Chem. Plasma Process. 23 (2003) 1-46.

[2] B. Jiang, J. Zheng, S. Qiu, M. Wu, Q. Zhang, Z. Yan, Q. Xue, Review on electrical discharge plasma technology for wastewater remediation, Chem. Eng. J. 236 (2014) 348-368.

[3] I. Adamovich, S. D. Baalrud, A. Bogaerts, P. J. Bruggeman, M. Cappelli, V. Colombo, U. Czarnetzki, U. Ebert, J. G. Eden, P. Favia, D. B. Graves, S. Hamaguchi, G. Hieftje, M. Hori, I. D. Kaganovich, U. Kortshagen, M. J. Kushner, N. J. Mason, S. Mazouffre, S. M. Thagard, H.-R. Metelmann, A. Mizuno, E. Moreau, A. B. Murphy, B. A. Niemira, G. S. Oehrlein, Z. Lj Petrovic, L. C. Pitchford, Y.-K. Pu, S. Rauf, O. Sakai, S. Samukawa, S. Starikovskaia, J. Tennyson, K. Terashima, M. M. Turner, M. C. M. van de Sanden, A. Vardelle, The 2017 Plasma Roadmap: Low temperature plasma science and technology, J. Phys. D: Appl. Phys. 50 (2017) 323001-1-46.

[4] H. Uchiike, T. Hirakawa, Color Plasma Displays, Proc. IEEE 90 (2002) 533-539.

[5] J. P. Boeuf, Plasma display panels: physics, recent developments and key issues, J. Phys. D: Appl. Phys. 36 (2003) R53-R79.

[6] L. F. Weber, History of the Plasma Display Panel, IEEE Trans. Plasma Sci. 34 (2006) 268-278.

[7] T. Shiga, L. C. Pitchford, J. P. Boeuf, S. Mikoshiba, Study of efficacy in a mercury-free at discharge fluorescent lamp using a zero-dimensional positive column model, J. Phys. D: Appl. Phys. 36 (2003) 512-521.

[8] K. Awamoto, H. Hirakawa, B. Guo, T. Shinoda, Current Status of the Flexible Surface Light Source Development using LAFi Technology, in: Proc. 22th Int. Disp. Workshops, vol. 1, 2015, pp. 619-620.

[9] S.-J. Park, C. M. Herring, A. E. Mironov, J. H. Cho, J. G. Eden, 25 W of average power at 172 nm in the vacuum ultraviolet from flat,

efficient lamps driven by interlaced arrays of microcavity plasmas, APL Photonics 2 (2017) 041302-1-7.

[10] S. Al-Gharabli, P. Engeβer, D. Gera, S. Klein, T. Oppenländer, Engineering of a highly efficient $Xe_2{}^*$-excilamp (xenon excimer lamp, $\lambda_{max} = 172$ nm, $\eta = 40$ %) and qualitative comparison to a low-pressure mercury lamp (LP-Hg, $\lambda = 185/254$ nm) for water purification, Chemosphere 144 (2016) 811-815.

[11] T. Zukawa, Y. Sasaki, H. Tsujimoto, N. Kamiko, E. Nakamura, Development of a mercury-free plate-type ultraviolet light source, Proc. Int. Ultraviolet Assosi. World Congr. (2016).

[12] R. Prakash, A. M. Hossain, U. N. Pal, N. Kumar, K. Khairnar, M. K. Mohan, Dielectric Barrier Discharge based Mercury-free plasma UV-lamp for efficient water disinfection, Sci. Rep. 7 (2017) 17426-1-8.

[13] C. Hoelen, P. Antonis, D. de Boer, R. Koole, S. Kadijk, Y. Li, Progress in extremely high brightness LED-based light sources, Proc. SPIE 10378 (2017) 103780N-1-19.

[14] M. Schratz, C. Gupta, T. J. Struhs, K. Gray, Reducing energy and maintenance costs while improving light quality and reliability with LED lighting technology, Conf. Rec. 2013 Annu. IEEE Pulp Paper Ind. Tech. Conf. (2013) 43-49.

[15] J. Meunier, Ph. Belenguer, J. P. Boeuf, Numerical model of an ac plasma display panel cell in neon-xenon mixtures, J. Appl. Phys. 78 (1995) 731-745.

[16] G. Oversluizen, T. Dekker, M. F. Gillies, S. T. de Zwart, High-Xe-content high-efficacy PDPs, J. Soc. Inf. Disp. 12 (2004) 51-55.

[17] Z. Liu, W.-B. Hu, C.-L. Liu, Luminance and Luminous Efficacy Improvement of Mercury-Free Flat Fluorescent Lamp With Arclike Electrode, IEEE Trans. Plasma Sci. 38 (2010) 2860-2866.

[18] H. Uchiike, K. Miura, N. Nakayama, T. Shinoda, Y. Fukushima, Secondary Electron Emission Characteristics of Dielectric Materials in AC-Operated Plasma Display Panel, IEEE Trans. Electron Devices 23 (1976) 1211-1217.

[19] B. Baumeier, P. Krüger, J. Pollmann, Bulk and surface electronic structures of alkaline-earth metal oxides: Bound surface and image-potential states from first principles, Phys. Rev. B 76 (2007) 205404-1-9.

[20] H. D. Hagstrum, Theory of Auger Neutralization of Ions at the Surface of a Diamond-Type Semiconductor, Phys. Rev. 122 (1961) 83-113.

[21] M. O. Aboelfotoh, J. A. Lorenzen, Influence of secondary-electron emission from MgO surfaces on voltage-breakdown curves in Penning mixtures for insulated-electrode discharges, J. Appl. Phys. 48 (1977) 4754-4759.

[22] G. Pacchioni, C. Sousa, F. Illas, F. Parmigiani, P. S. Bagus, Measures of ionicity of alkaline-earth oxides from the analysis of *ab initio* cluster wave functions, Phys. Rev. B 48 (1993) 11573-11582.

[23] G. Pacchioni, J. M. Ricart, F. Illas, Ab Initio Cluster Model Calculations on the Chemisorption of CO_2 and SO_2 Probe Molecules on MgO and CaO (100) Surfaces. A Theoretical Measure of Oxide Basicity, J. Am. Chem. Soc. 116 (1994) 10152-10158.

[24] M. B. Jensen, L. G. M. Pettersson, O. Swang, U. Olsbye, CO_2 Sorption on MgO and CaO Surfaces: A Comparative Quantum Chemical Cluster Study, J. Phys. Chem. B 109 (2005) 16774-16781.

[25] M. Sakai, S. Hatta, Y. Fukui, Y. Honda, M. Okafuji, Y. Yamauchi, M. Nishitani, Y. Tanaka, Analysis of the Deterioration of Secondary Electron Emission Coefficient of Protective Layers Formed by Alkaline-Earth Oxides for Plasma Display Panels, in: Proc. 15th Int. Disp. Workshops, vol. 3, 2008, pp. 1881-1884.

[26] Q. Yan, K. Kotera, H. Zhao, H. Liu, H. Zhou, Y. Tang, X. Deng, Calcium Magnesium Oxide Nano-crystal (Nano-CMO) for Improving Uniformity of High Xe Content PDP, SID Int. Symp. Dig. Tech. Pap. 45 (2014) 208-211.

[27] C.-S. Park, E. Y. Jung, H.-S. Tae, Improvement of luminous efficiency using Li-doped MgO layer coated by MgCaO crystal powders in plasma display panels, Mol. Cryst. Liq. Cryst. 645 (2017) 130-137.

[28] E. Takeda, T. Zukawa, T. Tsujita, K. Yoshino, Y. Morita, Annealing process for recovery of carbonated (Mg,Ca)O protective layer for plasma discharge device, Jpn. J. Appl. Phys. 57 (2018) 096001-1-7.

[29] T. Shinoda, H. Uchiike, S. Andoh, Low-Voltage Operated AC Plasma-Display Panels, IEEE Trans. Electron Devices 26 (1979) 1163-1167.

[30] S.-K. Kwon, S.-S. Yang, J.-H. Kim, B.-H. Ha, C.-H. Bae, J.-W. Seo, J.-W. Woo, J.-S. Ahn, Y.-L. Cho, Y.-K. Jung, S.-G. Choi, High Luminous Efficacy and Low Power Consumption Plasma TV, SID Int. Symp. Dig. Tech. Pap. 42 (2011) 741-744.

[31] K. A. Lee, B. K. Min, Y. S. Byeon, J. H. Choi, R. J. Jung, H. S. Uhm, E. H. Choi, Measurement of Energy Band Structure of MgO, MgSrO and MgCaO Thin Film by their Secondary Electron Emission Coefficient due to Auger Neutralization, J. Phys.: Conf. Ser. 417 (2013) 012009-1-11.

[32] R. Kim, Y. Kim, J. Cho, J.-W. Parka, Luminous efficiency and secondary electron emission characteristics of alternating current plasma display panels with MgO-SrO-CaO protective layers, J. Vac. Sci. Technol. A 18 (2000) 2493-2496.

[33] H. K. Yu, W.-K. Kim, J.-L. Lee, J. S. Kim, J. H. Ryu, The Effect of Doping to MgO Protection Layer on Secondary Electron Emission Property, SID Int. Symp. Dig. Tech. Pap. 37 (2006) 544-546.

[34] H. Uchiike, K. Sakiya, T. Hashimoto, T. Shinoda, Y. Fukushima, Optimum Composition of CaO, SrO Dielectric Materials in AC Plasma Display Panels, IEEE Trans. Electron Devices 30 (1983) 1735-1742.

[35] Y. Fukui, Y. Honda, Y. Yamauchi, M. Okafuji, M. Sakai, M. Nishitani, Y. Takata, Discharge properties and chemical stability of SrZrO films, J. Soc. Inf. Disp. 18 (2010) 1090-1094.

[36] Y. Yamauchi, Y. Fukui, Y. Honda, M. Okafuji, M. Sakai, M. Nishitani, Y. Yamauchi, Effect of Impurity in Discharge Gas on High γ Properties of Newly Developed CeSrO Film for Novel Plasma Display Panel, IEICE Trans. Electron. E95-C (2012) 1761-1768.

[37] M. Amatsuchi, A. Hirota, H. Lin, T. Naoi, E. Otani, H. Taniguchi, K. Amemiya, Discharge Time Lag Shortening by Using a New Material

Layer in AC PDP, in: Proc. 12th Int. Disp. Workshops, vol. 1, 2005, pp. 435-438.

[38] P. E. Larson, M. A. Kelly, Surface charge neutralization of insulating samples in x-ray photoemission spectroscopy, J. Vac. Sci. Technol. A 16 (1998) 3483-3489.

[39] D. A. Shirley, High-Resolution X-Ray Photoemission Spectrum of the Valence Bands of Gold, Phys. Rev. B 5 (1972) 4709-4714.

[40] E. Leyssenne, N. Sewraj, N. Merbahi, F. Marchal, M. C. Bordage, Visible and near infrared optical emission spectroscopic analysis of a pure xenon mono-filamentary dielectric barrier discharge, Proc. 31st Int. Conf. Phenom. Ionized Gases (2013).

[41] Y. Motoyama, D. Kato, N. Saito, M. Seki, Carbonation reaction of (Ca, Mg)O protective layer on plasma display panel, J. Soc. Inf. Disp. 21 (2013) 41-45.

[42] A. Galdikas, L. Praniavichius, Interactions of Ions with Condensed Matter, Horizons in World Physics Vol. 229, Nova Science Publishers, Inc., New York, 2000, Chap. 2.

[43] Y. K. Shin, J. K. Lee, C. H. Shon, W. Kim, Ion Energy Distribution in Alternating-Current Plasma Display Panel Cell, Jpn. J. Appl. Phys. 38 (1999) L174-L177.

[44] G. J. M. Hagelaar, G. M. W. Kroesen, M. H. Klein, Energy distribution of ions and fast neutrals in microdischarges for display technology, J. Appl. Phys. 88 (2000) 2240-2245.

[45] L. C. Pitchford, J. Wang, D. Piscitelli, J. P. Boeuf, Ion and Neutral Energy Distributions to the MgO Surface and Sputtering Rates in Plasma Display Panel Cells, IEEE Trans. Plasma Sci. 34 (2006) 351-359.

[46] S. J. Yoon, I. Lee, Theory of the lifetime of the MgO protecting layer in ac plasma display panels, J. Appl. Phys. 91 (2002) 2487-2492.

[47] W. D. Davis, T. A. Vanderslice, Ion Energies at the Cathode of a Glow Discharge, Phys. Rev. 131 (1963) 219-228.

[48] D. Piscitelli, A. V. Phelps, J. de Urquijo, E. Basurto, L. C. Pitchford, Ion mobilities in Xe/Ne and other rare-gas mixtures, Phys. Rev. E 68 (2003) 046408-1-10.

[49] K. Yoshino, K. Nomoto, M. Goto, R. Murai, T. Tsujita, M. Terauchi, Y. Morita, M. Nishitani, M. Kitagawa, Effects of Ne/Xe Gas Mixture Ratio on Sputtering Rate of MgO Protective Layer, in: Proc. 18th Int. Disp. Workshops, vol. 2, 2011, pp. 689-692.

[50] K. Hine, S. Yoshimura, K. Ikuse, M. Kiuchi, J. Hashimoto, M. Terauchi, M. Nishitani, S. Hamaguchi, Experimental evaluation of MgO sputtering yields by monochromatic Ne, Kr, or Xe ion beams, Thin Solid Films 517 (2008) 835-840.

[51] S. Yoshimura, K. Hine, M. Kiuchi, J. Hashimoto, M. Terauchi, Y. Honda, M. Nishitani, S. Hamaguchi, Experimental evaluation of CaO, SrO and BaO sputtering yields by Ne^+ or Xe^+ ions, J. Phys. D: Appl. Phys. 44 (2011) 255203-1-5.

[52] S. Yoshimura, K. Hine, M. Kiuchi, J. Hashimoto, M. Terauchi, Y. Honda, M. Nishitani, S. Hamaguchi, Sputtering Yields of CaO, SrO, and BaO by Monochromatic Noble Gas Ion Bombardment, Jpn. J. Appl. Phys. 51 (2012) 08HB02-1-4.

[53] https://www.bolsig.laplace.univ-tlse.fr/

[54] S. S. Yang, J. K. Lee, S. W. Ko, H. C. Kim, J. W. Shon, Two-Dimensional Kinetic and Three-Dimensional Fluid-Radiation Transport Simulations of Plasma Display Panel, Contrib. Plasma Phys. 44 (2004) 536-541.

[55] Q. Wei, K.-D. Li, J. Lian, L. Wang, Angular dependence of sputtering yield of amorphous and polycrystalline materials, J. Phys. D: Appl. Phys. 41 (2008) 172002-1-4.

[56] K. Ikuse, S. Yoshimura, M. Kiuchi, M. Terauchi, M. Nishitani, S. Hamaguchi, Sputtering yields of magnesium hydroxide [$Mg(OH)_2$] by noble-gas ion bombardment, J. Phys. D: Appl. Phys. 45 (2012) 432001-1-5.

[57] M. El Marsi, R. Moultif, S. Lahlou, S. Rochd, A. Dezairi, Monte Carlo simulations of MgO and $Mg(OH)_2$ thin films sputtering yields by noble-gas ion bombardment in plasma display panel PDP, Nucl. Inst. Methods Phys. Res. B 430 (2018) 72-78.

[58] G. Uchida, S. Uchida, T. Akiyama, H. Kajiyama, T. Shinoda, Effect of high Xe-concentration in a plasma display panel with a SrCaO cold cathode, J. Appl. Phys. 107 (2010) 103311-1-7.

[59] D. Zhu, L. Song, X. Zhang, H. Kajiyama, Vacuum ultra-violet emission of plasma discharges with high Xe partial pressure using a cathode protective layer with high secondary electron emission, J. Appl. Phys. 115 (2014) 063302-1-7.

[60] S. Rauf, M. J. Kushner, Dynamics of a coplanar-electrode plasma display panel. II. Cell optimization, J. Appl. Phys. 85 (1999) 3470-3476.

[61] K. C. Choi, N. H. Shin, K. S. Lee, B. J. Shin, S.-E. Lee, Study of Various Coplanar Gaps Discharges in ac Plasma Display Panel, IEEE Trans. Plasma Sci. 34 (2006) 385-389.

[62] S. Hori, T. Murakoso, E. Otani, K. Amemiya, R. Murai, Improvement of Luminous Efficiency Using New Structure in AC-PDPs, SID Int. Symp. Dig. Tech. Pap. 42 (2011) 745-747.

[63] S. B. Shim, S.-Y. Cho, D. K. Lee, I. C. Song, C. H. Park, H.-J. Lee, H. J. Lee, The effects of permittivity and thickness of dielectric layers on micro dielectric barrier discharges, Thin Solid Films 518 (2010) 3037-3041.

[64] P. Zhang, Y. Tu, L. Yang, Simulation studies of the dielectric layer effect on the discharge characteristics of the shadow mask plasma display panel, J. Vac. Sci. Technol. B 29 (2011) 04E105-1-5.

[65] E. Takeda, T. Zukawa, T. Ishibashi, K. Yoshino, Y. Morita, M. Fujii, Mechanisms for the degradation of phosphor excitation efficiency by short wavelength vacuum ultraviolet radiation in plasma discharge devices, J. Phys. Chem. Solids 124 (2019) 274-280.

[66] C. H. Ha, B. Y. Han, J. S. Yoo, H. S. Bae, K.-W. Whang, Characteristics of Phosphor Degradation in AC-Driven Plasma Display Panels, J. Electrochem. Soc. 155 (2008) J230-J234.

[67] K. Sawada, S. Adachi, Unique photoluminescence degradation/recovery phenomena in trivalent ion-activated phosphors, J. Appl. Phys. 118 (2015) 103106-1-7.

[68] L. Amidani, K. Korthout, J. J. Joos, M. van der Linden, H. F. Sijbom, A. Meijerink, D. Poelman, P. F. Smet, P. Glatzel, Oxidation and Luminescence Quenching of Europium in $BaMgAl_{10}O_{17}$ Blue Phosphors, Chem. Mater. 29 (2017) 10122-10129.

[69] H. K. Yu, W.-K. Kim, J.-L. Lee, E. C. Park, J. S. Kim, J. H. Ryu, Degradation Mechanism of Secondary Electron Emission in Plasma-Exposed MgO Films, Jpn. J. Appl. Phys. 48 (2009) 076003-1-4.

[70] C.-S. Park, H.-S. Tae, E.-Y. Jung, J. H. Seo, B. J, Shin, Influence of Ion Bombardment on Electron Emission of MgO Surface in AC Plasma Display Panel, IEEE Trans. Plasma Sci. 38 (2010) 2439-2444.